Colloid Polym Sci 279: 312–322 (2001)

ORIGINAL CONTRIBUTION

The crystallization kinetics of polyamide-12

C. J. G. Plummer
J.-E. Zanetto
P.-E. Bourban
J.-A. E. Månson

Received: 9 March 2000
Accepted: 28 September 2000

C. J. G. Plummer · J.-E. Zanetto
P.-E. Bourban · J.-A. E. Månson (✉)
Laboratoire de Technologie des Composites et Polymères, Ecole Polytechnique Fédérale de Lausanne (EPFL)
1015 Lausanne, Switzerland
e-mail: jan-anders.manson@epfl.ch
Tel.: + 41-21-6935880
Fax: + 41-21-6934281

Abstract The crystallization kinetics of polyamide-12 has been investigated using a combination of differential scanning calorimetry (DSC) and hot-stage optical microscopy. The DSC data for isothermal crystallization were consistent with a simple two-parameter Avrami model for isothermal crystallization and optical measurements of the spherulite growth rates and nucleation density. On the basis of semi-empirical expressions for these quantities, it is shown that with small adjustments the model can also account for DSC data for nonisothermal crystallization, provided that corrections are made for the dynamic heat balance between the sample and the DSC oven.

Key words Polyamide-12 · Crystallization · Transmission electron microscopy · Solidification · Optical microscopy

Introduction

The aim of this work is to provide a working analytical description of the crystallization kinetics of polyamide-12 (PA-12) in the range of temperatures readily accessible to crystallization experiments in the differential scanning calorimeter and to hot-stage light microscopy. PA-12 has attracted considerable recent interest as a matrix for fibre-reinforced composites. As with any semicrystalline thermoplastic of commercial importance, a description of the parameters that govern its crystallization kinetics is of great interest, being central to any rational approach to thermomechanical processing.

At relatively high temperatures and under quiescent conditions, the crystallization of PA-12 from the melt proceeds by nucleation and growth of spherulites. If adequate descriptions of the nucleation rate, α, and the spherulite growth rate, G, are available, the crystallization kinetics may therefore be modelled using the classical approach often attributed to Avrami, but which was developed independently by a number of authors [1, 2, 3, 4, 5]. Alternatively, α and G may be inferred from the crystallization kinetics as reflected by differential scanning calorimetry (DSC) data, say. In this latter approach, apparent deviations from ideal Avrami behaviour are often accounted for by modifications to the model based on various hypotheses, such as that of secondary crystallization behind the spherulite growth front [6]. It should nevertheless be borne in mind that such deviations may also arise from extrinsic effects such as an inappropriate choice of sample geometry, and, particularly in nonisothermal experiments, from fluctuations in the sample temperature with respect to that of the DSC oven [7, 8].

In what follows, it is shown that given suitable experimental precautions and corrections, a combination of the basic Avrami model and measurements of G by hot-stage microscopy can provide an adequate description of both isothermal and nonisothermal DSC data for PA-12. The extent to which it is possible to extrapolate the results to conditions difficult to access using conventional techniques is then examined.

Experimental

Materials

Ems Chemie provided the PA-12 for this study in the form of extruded pellets with a weight-average molar mass of 26.4 kgmol^{-1} and a number-average molar mass of 15.7 kgmol^{-1}.

Differential scanning calorimetry

Samples for DSC with a mass of approximately 2 mg were cut from a 500-μm-thick compression moulded sheet and pressed into aluminium sample pans with pierced covers. The measurements were carried out under dry nitrogen gas using a Perkin-Elmer DSC 7, with the block held at −30 °C. The temperature scale of the differential scanning calorimeter was calibrated with indium and zinc, which were heated at various constant rates. The onset temperatures of the observed melting endotherms were then extrapolated to zero heating rate in order to obtain the value of the melting point, T_m, required for the calibration. The heat transfer coefficient, γ, between the sample pan and the DSC oven was determined to be approximately 1.4×10^{-2} WK^{-1} from the melting endotherm of indium as described elsewhere [7, 8, 9].

In order to obtain reproducible measurements, all the PA-12 samples were held at 220 °C for 30 s prior to isothermal crystallization or cooling in the differential scanning calorimeter. Under these conditions, repeated cycles of melting and crystallization gave very similar data for a given crystallization temperature or cooling rate, even for a relatively large number of cycles. The previous crystallization temperature also had little influence on the data. Nevertheless, as a precaution, the samples were changed every six cycles. After the measurements each sample was removed from its pan in order to check that its geometry had not altered substantially during melting and to examine its microstructure.

A typical isothermal crystallization cycle consisted of melting at 220 °C for 30 s, cooling at a nominal rate of 100 Ks^{-1} to the required crystallization temperature, isothermal crystallization, cooling to 50 °C at 100 Ks^{-1} and reheating to 220 °C at a constant rate. The melting endotherm was recorded during each heating step. T_m for the PA-12 was then determined by extrapolating the melting-peak temperatures obtained at different heating rates to zero heating rate. Baselines for the isothermal part of the cycles were estimated from runs in which the temperature of the isothermal step was 180 °C. At this temperature the crystallization rate was too low for it to contribute significantly to the signal. In the nonisothermal crystallization cycles, after melting at 220 °C, the samples were cooled directly to 50 °C at the required rate.

Hot-stage microscopy

Hot-stage microscopy was carried out using a Linkam THMS 600 hot stage mounted on an Olympus OM2 light microscope equipped with crossed polarizers. Films with thicknesses of several microns were cast onto a glass cover slip from freshly made up solutions of PA-12 in phenol at 50 °C and were dried under vacuum at the same temperature. Observations were carried out under nitrogen with a second cover slip placed over the film to limit degradation and dewetting. A melting temperature of 220 °C was used for all the experiments, and the spherulite growth rates were measured from video recordings of isothermal crystallization at the required temperature. The nucleation density in these films was generally sufficiently low for spherulites of up to several hundred microns in diameter to be formed. In each case isothermal conditions were assumed to be reflected by a time-independent growth rate. To achieve this at temperatures where the overall crystallization rate was relatively rapid (below about 150 °C), films were cast from 15% PA-12/polystyrene in *m*-cresol. Crystallization of certain of the dispersed domains of the PA-12 that resulted was delayed long enough for growth to be observable under isothermal conditions in this temperature regime.

Microstructural characterization

To estimate spherulite sizes a number of samples were embedded in epoxy resin after crystallization in the differential scanning calorimeter and sections of a few microns in thickness were prepared using a glass knife and a Reichert–Jung Ultracut-E ultramicrotome. Figure 1 is from a sample crystallized isothermally in the differential scanning calorimeter at 170 °C and shows a uniform distribution of equiaxed spherulites. Since the spherulites were relatively ill defined no attempt was made at a detailed morphological analysis. Rather, the average spherulite radius was estimated to be half the average centre-to-centre distance of neighbouring spherulite sections, divided by a factor of 0.8 to correct for the presence of nondiametral sections (the spherulite radii were typically much greater than the film thickness). Ultrathin sections (about 100 nm in thickness) were obtained at room temperature using a Reichert–Jung Ultracut-E ultramicrotome with a 30° diamond knife, after fixing and staining by overnight exposure to RuO_4 vapour. The best results were obtained by repeating this procedure at least once. The sections were observed using a Philips EM430 transmission electron microscope (TEM) at 300 kV in bright field.

Analysis

Isothermal crystallization

The Avrami model may be used to describe space filling by an array of similar objects nucleating at random points in space whose size changes at a well-defined rate, subject to the condition that they cannot nucleate in a region already occupied by another object. In the ideal case of spherical objects with a radial growth rate G and nucleating at a rate α, the degree of conversion, X, after time t is [4]

$$X(t) = 1 - \exp\left[-\frac{4\pi}{3}\int_0^t \alpha(\varsigma)\left(\int_\varsigma^t G(\xi)\mathrm{d}\xi\right)^3 \mathrm{d}\varsigma\right]. \qquad (1)$$

Under isothermal conditions, for which G is generally observed to be constant in polymers, this simplifies to

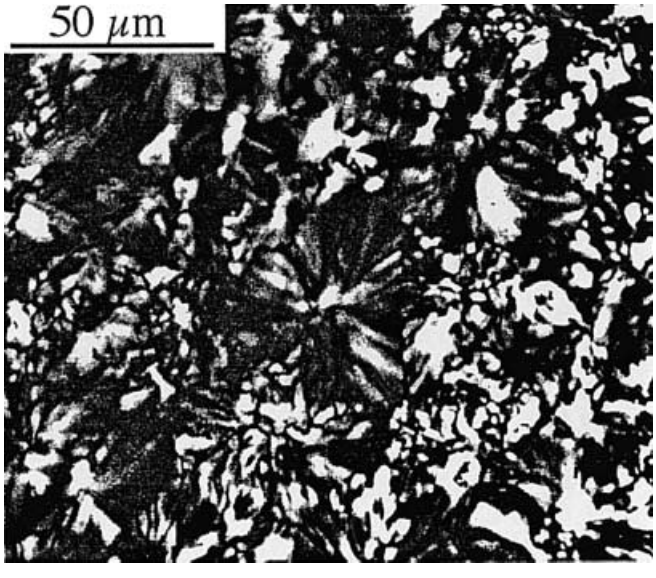

Fig. 1 Optical micrograph of polyamide-12 (PA-12) crystallized isothermally in the differential scanning calorimeter at 170 °C and viewed between crossed polarizers

$$X(t) = 1 - \exp\left[-\frac{4\pi G^3}{3}\int_0^t \alpha(\varsigma)(t-\varsigma)^3 \mathrm{d}\varsigma\right]. \quad (2)$$

This expression can be simplified further in the case of instantaneous heterogeneous nucleation at $t = 0$ to give

$$X(t) = 1 - \exp\left[-\frac{4\pi G^3}{3} N_o t^3\right], \quad (3)$$

where N_o is the number of nuclei per unit volume. However, even for heterogeneous nucleation there is often a significant activation barrier. A single activation barrier may be characterized by a time constant, τ, and a first-order rate equation may be used to describe isothermal nucleation [3],

$$N(t) = N_o\left[1 - \exp\left(-\frac{t}{\tau}\right)\right], \quad (4)$$

from which $\alpha(t)$ may be obtained by differentiation. More generally, there is likely to be a spread in nucleation times, reflected by a sigmoidal form for $N(t)$; however, if this spread is very much less than the total crystallization time, it is reasonable to assume a single "induction" time and to replace Eq. (3) by

$$X(t) = 1 - \exp\left[-\frac{4\pi G^3}{3} N_o (t-\tau)^3\right]; t \geq \tau,$$
$$X(t) = 0; t < \tau. \quad (5)$$

The spherulites in Fig. 1 represented the upper limit of the observed size range, as discussed later. Their mean radii were about 50 μm and there were consequently at least ten spherulites per unit sample thickness and more than 10^3 spherulites per sample. Truncation effects were therefore insignificant and the use of the Poisson approximation implicit in Eq. (5) was justified. There is also some suggestion in Fig. 1 of approximately planar interspherulite boundaries locally, which would be consistent with a single induction time; however this was difficult to confirm from micrographs taken at higher undercooling and N_o was found to vary significantly with temperature, as inferred both from comparison of the DSC data with direct measurements of G and from direct examination of the samples. Nonetheless, a dependence of N_o on T need not be incompatible with the notion of predetermined nucleation under isothermal conditions and at relatively large undercooling [10, 11].

Nonisothermal crystallization

The DSC signal is equal to $\gamma(T_s - T_f)$, where T_s is the sample temperature, T_f is the oven temperature of the calorimeter and γ is the heat transfer coefficient referred to in the Experimental section. As long as the sample mass does not exceed a few milligrams, variations in the difference between T_s and T_f during isothermal crystallization lead to minor corrections and are generally ignored. In a nonisothermal experiment, on the other hand, $\gamma(T_s - T_f)$ may be nonnegligible even in the absence of a phase change. For a constant cooling rate and steady state conditions, the difference between T_s and T_f is constant and can be determined from the shifts in a suitable transition at different cooling or heating rates. However, the evolution of T_s at high cooling rates is also significantly influenced by the evolution of latent heat during crystallization. This is nevertheless relatively straightforward to correct for, if the crystallization kinetics and the heat of crystallization are known [7, 8, 9].

The model used here for nonisothermal crystallization is based on similar approximations to those used for the isothermal case. Equation (1) is replaced by

$$X(t) = 1 - \exp\left[-\frac{4\pi}{3} N_o(\tau_d)\left(\int_{\tau_d}^t G(\xi)\mathrm{d}\xi\right)^3\right]; t \geq \tau_d,$$
$$X(t) = 0; t < \tau_d, \quad (6)$$

where τ_d is a dynamic induction time. Rather than determine τ_d explicitly, nucleation was assumed to occur at a sample temperature T_{sd}, defined by

$$1 = \int_{T_0}^{T_{sd}} \frac{1}{\dot{\theta}\tau(T_s)}\mathrm{d}T_s, \quad (7)$$

where T_0 is the sample temperature at $t = 0$ and $\dot{\theta}$ is the cooling rate (initial transients were ignored). N_o was then taken to be $N_o(T_{sd})$, which was obtained by interpolation or extrapolation of data from isothermal crystallization. In practice, however, both N_o and T_{sd} were adjusted in order to optimize the fit to the data. This may have compensated inaccuracies (see later), but slight adjustment of N_0 was in any case anticipated to be necessary since T_s typically decreased by up to a few Kelvin during nonisothermal crystallization. This would lead to a somewhat higher effective value of N_o than that predicted at T_{sd}.

DSC cooling curves were simulated by solving numerically the heat balance equation,

$$\gamma(T_s - T_f) = -\left(m_s C_s + m_p C_p\right)\frac{\mathrm{d}T_s}{\mathrm{d}t} + m_s \Delta H_s \frac{\mathrm{d}X}{\mathrm{d}t}, \quad (8)$$

where C_s and C_p are the heat capacities of the sample and the sample pan (taken to be 1.8 [12] and 0.9 $\mathrm{JK^{-1}g^{-1}}$, respectively), m_s is the sample mass, m_p is the mass of the sample pan (about 30 mg) and ΔH is the enthalpy of fusion per unit mass of the sample, which decreased from about 80 to 60 $\mathrm{Jg^{-1}}$ as the cooling rate was raised from 1 to 40 $\mathrm{Kmin^{-1}}$ as shown in Fig. 2. Details of our own implementation of this method are given elsewhere [9].

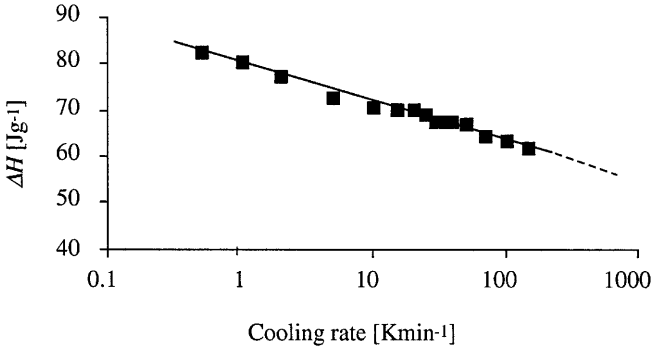

Fig. 2 Differential scanning calorimetry (DSC) data for the crystallization enthalpy of PA-12, ΔH, as a function of cooling rate

Results and discussion

An isothermal crystallization curve with relatively strong baseline curvature is shown in Fig. 3 in order to illustrate the baseline correction. A correction for the difference in heat capacity, ΔC_s, between the amorphous and crystalline phases was also made as follows. A first estimate of the degree of conversion was obtained from

$$x = \frac{\int_0^t W_b(\xi)\mathrm{d}\xi}{\int_0^{t_{end}} W_b(\xi)\mathrm{d}\xi}, \quad (9)$$

where W_b is the baseline-subtracted signal and t_{end} is a first estimate of the endpoint of the crystallization. The corrected signal, W, was taken to be $W_b - xm_s\Delta C_s\dot{\theta}$, where ΔC_s was adjusted so that W tended to zero for $t \gg t_{end}$. The degree of conversion, X, was then determined from Eq. (9) by replacing W_b by W.

Equation (5) was fitted to $X(t)$ by adjusting $K = 4/3\pi N_0 G(T)^3$ and τ. As shown in Fig. 3, there were slight discrepancies at small $X(t)$, which were expected in view of the approximate treatment of the nucleation kinetics, but the overall agreement was satisfactory. The values of $K(T)$ and $\tau(T)$ obtained in this way are summarized in Fig. 4. The data for G from hot-stage observations at different temperatures are shown in Fig. 5. These were combined with the data in Fig. 4 in order to estimate the effective nucleation density, N_o, in the DSC samples. The results are shown in Fig. 6, illustrating the significant decrease in N_0 with decreasing T referred to earlier.

The calculation of the results in Fig. 6 required interpolation of the G data since the temperatures at which the measurements were made did not always coincide with those of the DSC measurements. An

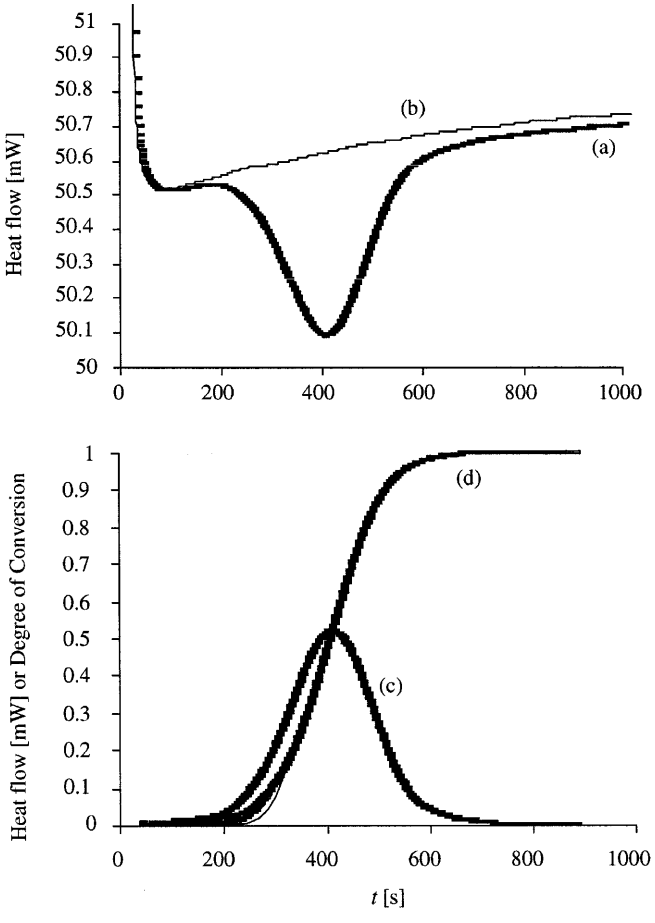

Fig. 3 *a* Isothermal crystallization curve at $T_c = 165$ °C, *b* estimated baseline, *c* $W(t)$ after baseline correction and correction for ΔC_s, *d* $X(t)$ (*bold curve*) superposed onto an empirical fit of Eq. (5) to the data

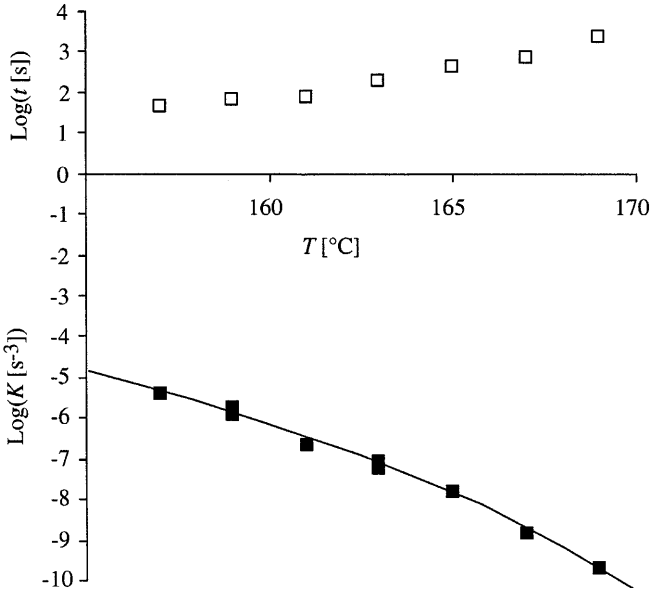

Fig. 4 $K = 4/3\pi N_o G(T)^3$ (*filled squares*) and $\tau(T)$ (*open squares*), determined by fitting Eq. (5) to the isothermal DSC data. The curves are derived from the analytical expressions for $\tau(T)$, $N_o(T)$ and G(T) described in the text

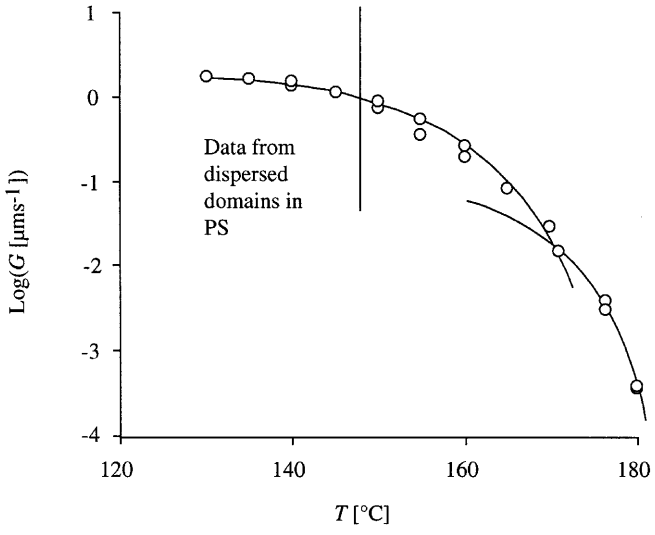

Fig. 5 $G(T)$ determined by hot-stage optical microscopy. Data points in the range indicated were obtained from blends as described in the text. The curves are fits of Eq. (10) to the data (see Fig. 8)

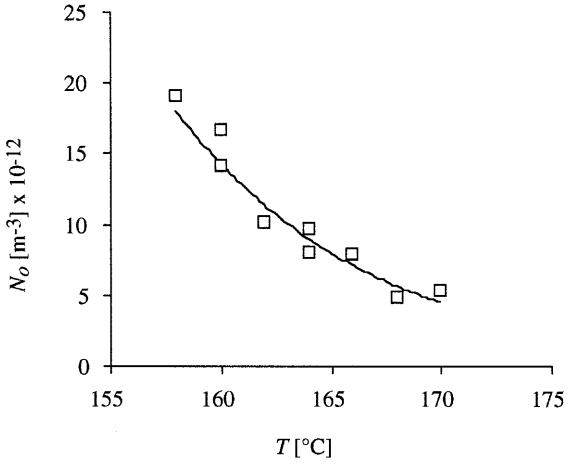

Fig. 6 $N_o(T)$ estimated from the results for K in Fig. 4 and the data for G in Fig. 5, along with the exponential fit initially used to extrapolate to lower temperatures

analytical description for G was also necessary for modelling the nonisothermal crystallization curves. For this purpose expressions derived from the Lauritzen and Hoffman (LH) theory were used [13]. These take the form

$$G = G_0 \exp\left(-\frac{U}{R(T - T_0)}\right) \exp\left(-\frac{K_G}{T\Delta T}\right), \qquad (10)$$

where G_0 and K_G are constants. The first exponential term is a transport term and, following Hoffman et al., the "universal" values $U = 6270$ Jmol^{-1} and $T_0 = T_g - 51.2 \approx 264$ K were assumed [14, 15]. The case has also been made for a single temperature-independent activation energy [16] that is a universal function of the melting point and T_g [17], but here both forms of transport term led to very similar results in the temperature regime of interest. The dependence of the second exponential term on the supercooling, $\Delta T = T - T_{mo}$, where T_{mo} is the equilibrium melting point, is a more general feature of expressions for G. T_{mo} was estimated to be about 190 °C from T_m determined at different crystallization temperatures, T_c, using the Hoffman–Weeks construction [18] shown in Fig. 7. This compares with a literature value of 187 °C [19].

To determine G_0 and K_G, the data for G were linearized by plotting $\ln(G) + U/R(T-T_0)$ against $1/T\Delta T$ as shown in Fig. 8. It is clear from the figure that the data did not all lie on one straight line; however, a reasonable fit could be obtained by considering them to fall into two distinct "regimes". In the low-temperature regime K_G was about twice the value obtained in the high-temperature regime, suggesting there to be a transition from regime I to regime II, in terms of the LH theory, when the temperature decreased below about 171 °C. It is beyond the scope of this article to comment further on the existence of these regimes or on the validity of other aspects of the theory. Moreover, for the purpose of modelling nonisothermal crystallization in the differential scanning calorimeter in the range of cooling rates investigated here, it was sufficient to take $G_0 = 0.013$ ms^{-1} and $K_G = 80{,}000$ K^2 over the whole temperature range.

In calculating T_{sd} from Eq. (7) it was assumed that τ showed a similar temperature dependence to G, so

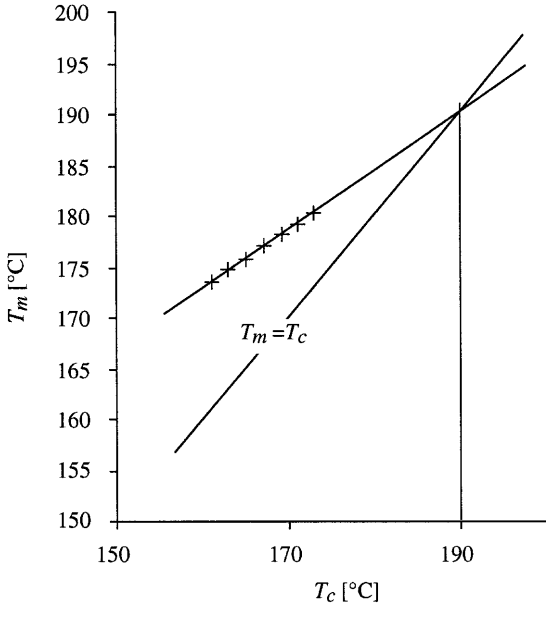

Fig. 7 Estimation of T_{mo} from data for $T_m(T_c)$. T_{mo} is given by the value of T_c at which the linear extrapolation of $T_m(T_c)$ crosses the curve $T_m = T_c$

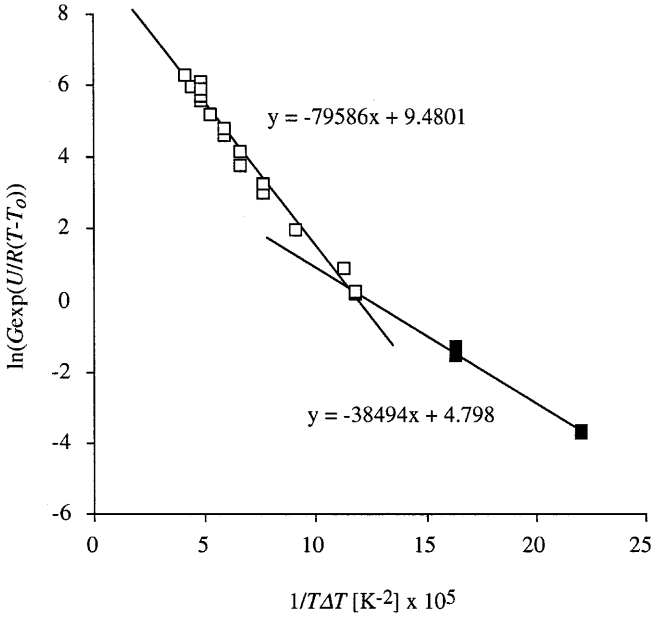

Fig. 8 Fits of Eq. (10) to data for G

$$\tau = \tau_0 \exp\left(\frac{U}{R(T - T_0)}\right) \exp\left(\frac{K_N}{T\Delta T}\right). \quad (11)$$

The fit of Eq. (11) to the data in Fig. 4 gave $\tau_o = 1.5 \times 10^{-4}$ s and $K_N = 110{,}000$ K^2 (cf. Eq. 10). The form of Eq. (11) was chosen somewhat arbitrarily, but it was found to account well for the observed temperature dependence of τ. (cf. the classical Turnbull–Fisher expression for primary nucleation, for example, in which the argument of the second exponential is raised to the power 2 [20]).

The data obtained from nonisothermal crystallization at 40 Kmin^{-1} are compared in Fig. 9 with curves calculated using parameters derived from the isothermal data (Fig. 6, Eqs. 9, 11) and a simulation made after adjusting N_o and T_{sd} to optimize the fit. Also shown is the optimized fit plotted as a function of the sample temperature, T_s, and the corresponding degree of conversion as a function of T_s. This demonstrates that crystallization itself took place over a relatively narrow range of sample temperatures between 140 and 146 °C, in spite of the fact that the oven temperature, T_f, corresponding to the end of the crystallization exotherm was about 132 °C. For nominal cooling rates above 40 Kmin^{-1} adequate control of the temperature ramp

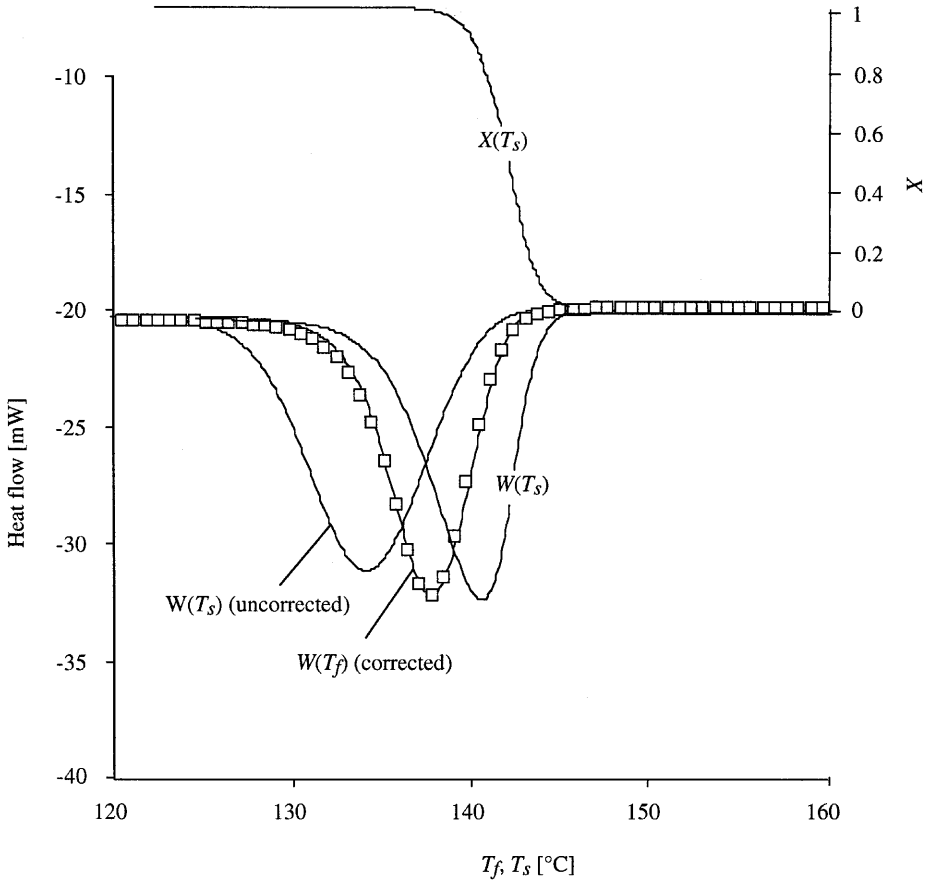

Fig. 9 Comparison of data (*open squares*) with a simulation of a nonisothermal cooling curve, $W(T_f)$, at 40 Kmin^{-1} made using N_o extrapolated from the data in Fig. 6 (uncorrected) and a simulation made after adjusting N_o and T_{sd} to optimize the fit to the data (corrected). Also shown is the adjusted simulation plotted as a function of the sample temperature, T_s, and the degree of conversion as a function of T_s

became difficult [9] and 146 °C was therefore considered to be the lower limit of the temperature range which could be investigated in detail.

DSC results for various cooling rates are shown in Fig. 10 along with the calculated curves. The adjusted values of $N_o(T_{sd})$ used to obtain these curves are compared with the results from isothermal experiments in Fig. 11 and the adjusted values of T_{sd} are compared with the predictions of Eqs. (9) and (11) in Fig. 12. The differences between the predicted and adjusted values of T_{sd} were comparatively small. The differences between the predicted $N_o(T_{sd})$ and adjusted values of N_0 were more significant, as borne out by Fig. 9. However the predicted values relied on a relatively long extrapolation of data points confined to a narrow range of temperatures in which N_o was changing relatively slowly with T. An exponential temperature dependence has been observed in other polymers [10, 11], but given the assumptions implicit in the use of Eq. (10) for G, corroborating evidence for the evolution in N_o from optical microscopy was considered to be important. The results of direct estimates of the average spherulite radii are shown in Fig. 13, where they are compared with the radius of a sphere with volume N_o^{-1}. The agreement is satisfactory, although in the case of the sample cooled at 40 $Kmin^{-1}$ it was difficult to characterize the morphology precisely, owing to overlap in the projections of individual spherulites and an ill-defined spherulitic texture.

Time–temperature transformation diagrams

Time–temperature transformation diagrams are a convenient way of representing either data or models for solidification. The isothermal time–temperature trans-

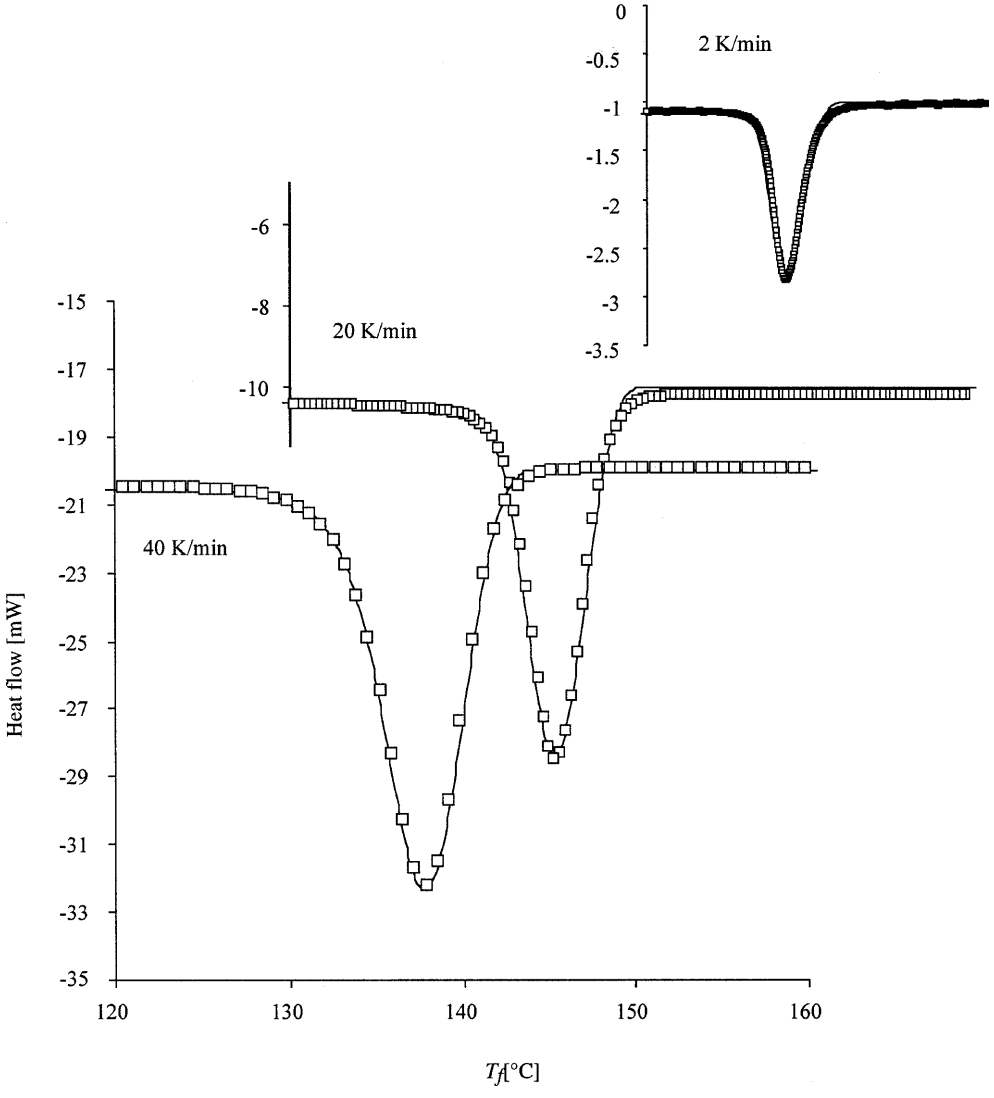

Fig. 10 Data for nonisothermal crystallization at various cooling rates (*open squares*) and simulated curves obtained by treating $N_o(T_{sd})$ and T_{sd} as adjustable parameters

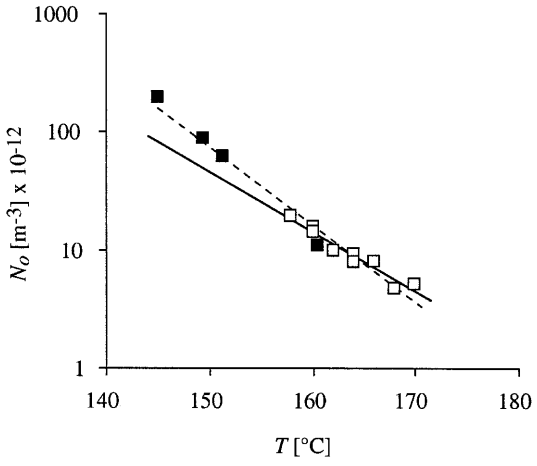

Fig. 11 $N_o(T)$ estimated from the isothermal data (*open symbols*), compared with results from fits to nonisothermal DSC data (*filled symbols*), along with an exponential fit to the isothermal results only (*solid line*) and a fit to all the results (*hatched line*)

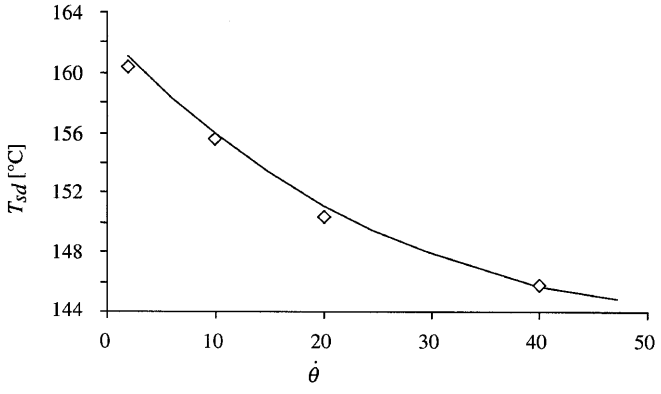

Fig. 12 Comparison of adjusted values of T_{sd} used for the fits in Fig. 10 with the predictions of Eqs. (9) and (11)

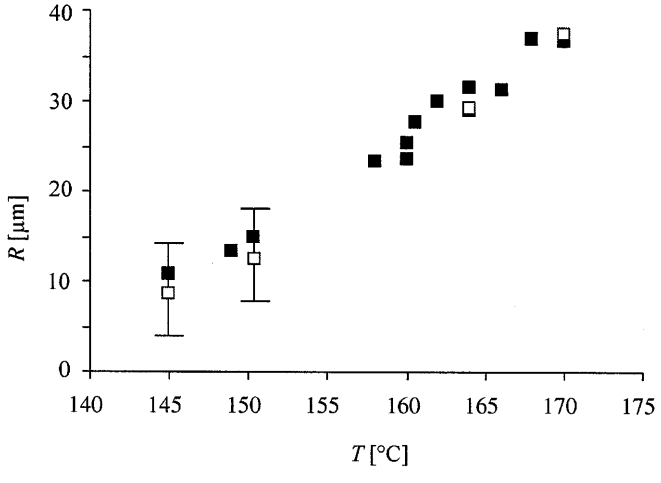

Fig. 13 Comparison of values of spherulite radii, R, inferred from the results for N_o with values estimated directly from thin sections (*open squares*)

formation diagram for PA-12 inferred from the present model and extrapolated to higher undercooling using $N_o = 9 \times 10^{41}\exp(-0.153T)$ (T in Kelvin) to interpolate and extrapolate $N_o(T)$ (the hatched curve in Fig. 11) is shown in Fig. 14. It should be emphasized that the induction time τ is not expected to correspond to a true onset since it is derived from a fit of a two-parameter Avrami model to data from a system in which the effective induction times may be distributed (and in which thermal nucleation may also be present). On the other hand, the curves for 50 and 99% conversion are realistic for the temperature range in which data were available.

Figure 15a shows the non-isothermal time–temperature conversion diagram for a starting temperature of 220 °C, chosen to be consistent with the DSC data (a different choice of starting temperature would simply result in a shift in the zero of the time axis). The curves were calculated from Eq. (6) and therefore do not include effects of latent heat evolution or thermal lag and will therefore, in general, not reflect the apparent behaviour in practical situations. Indeed, as indicated in Fig. 15a, the predicted time for 99% conversion diverged from the experimental DSC data quite markedly at the highest cooling rates, even when these latter were corrected for thermal lag. Nevertheless certain situations, such as quenching against a cold metallic mould, will be approximately consistent with the ideal case. Also shown for completeness in Fig. 15b is a time–temperature degree of crystallinity diagram, taking the enthalpy of crystallization of 100% crystalline sample to be 130 Jmol^{-1} [19] and using the data shown in Fig. 2.

The question naturally arises as to the extent to which the extrapolation of the present model to lower crystallization temperatures and/or faster solidification rates in Figs.14 and 15 is justified. The extrapolation of G is arguably physically based [13, 21], and the ΔT dependence is widely observed, even if reservations have been expressed regarding the form of the transport term. N_0, on the other hand, was interpolated/extrapolated assuming a simple exponential dependence on T inferred empirically from the results. There is therefore no a priori basis for assumptions about N_o in temperature regimes not accessible here. Also, even if it were possible to justify extrapolation of N_o measured at high and intermediate crystallization temperatures, in practice these latter are often strongly dependent on the thermomechanical history (other parameters may also vary, particularly in the presence of a flow field). Therefore, although the application of the present approach to well-controlled DSC experiments has been demonstrated, characterization of the microstructure after crystallization would still be necessary to verify any initial hypothesis regarding the nucleation density in other specific cases.

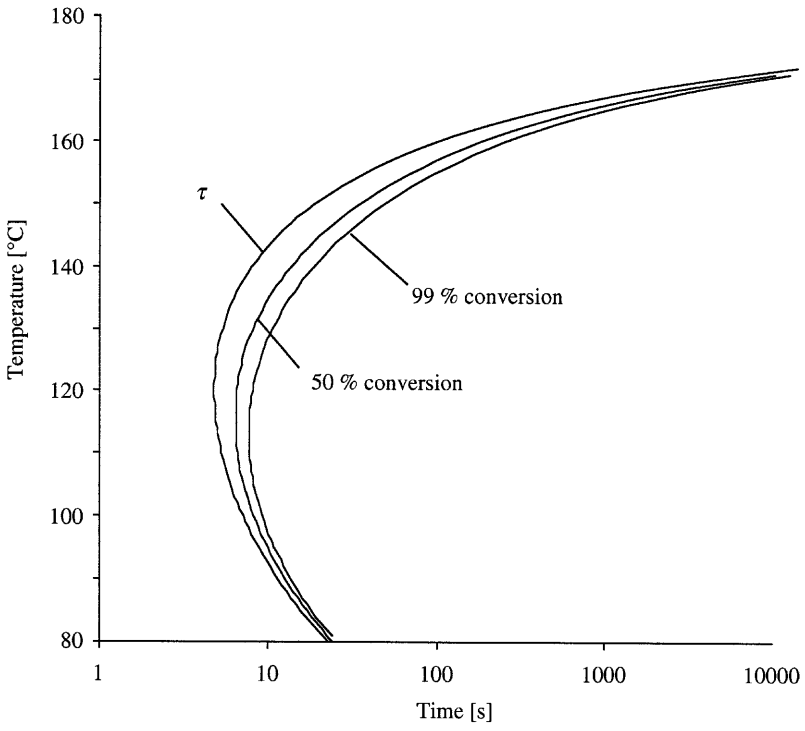

Fig. 14 Isothermal time–temperature transformation diagram for PA-12

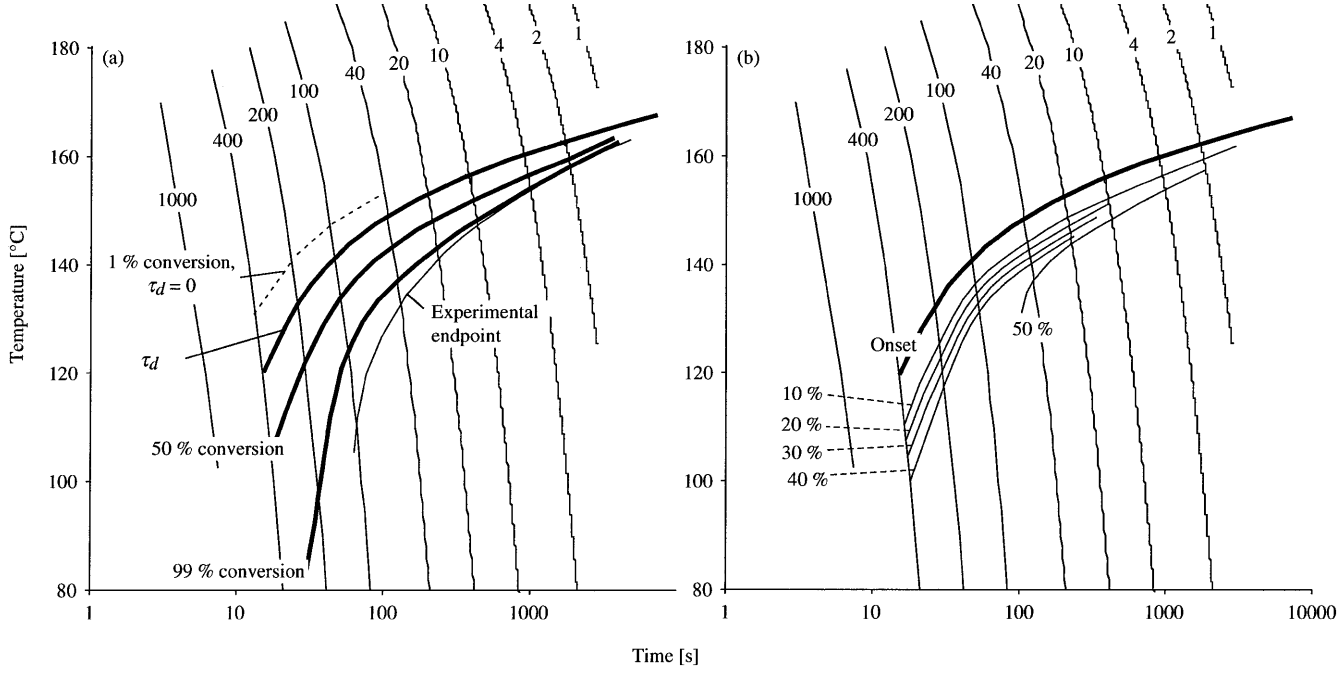

Fig. 15 Nonisothermal time–temperature transformation diagram for PA-12 showing **a** the degree of conversion and **b** the absolute degree of crystallinity (curves corresponding to cooling rates are indicated in Kelvin per minute)

In connection with this, the lamellar structures of various samples were investigated briefly. The microstructures of samples crystallized isothermally at different temperatures and that of a sample taken from close to the surface of a molten plaque brought into contact with a metallic surface held at room temperature are shown in Figs. 16 and 17. In this latter case, the spherulite envelopes were ill defined, although lower-magnification images of heavily irradiated samples suggested a mean radius of about 0.5 μm.

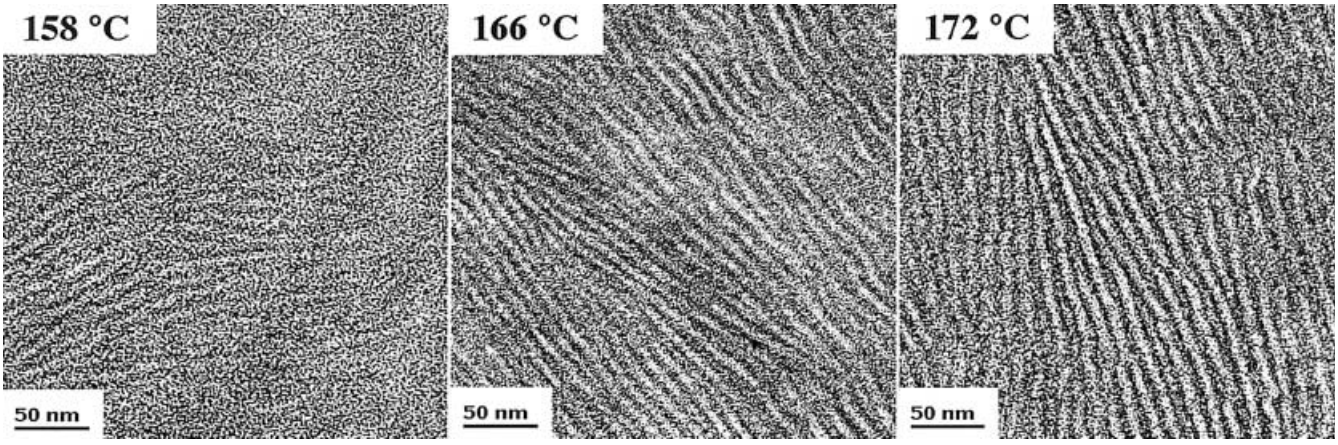

Fig. 16 Lamellar structure in samples isothermally crystallized at different temperatures as indicated

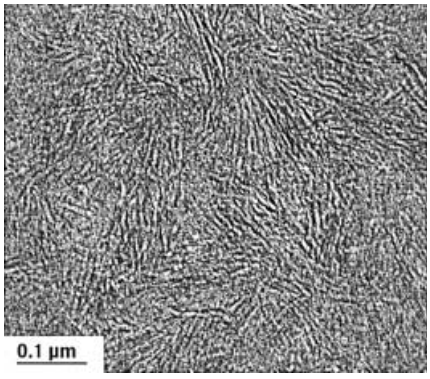

Fig. 17 Lamellar structure obtained by bringing the surface of a molten plaque into contact with a metal plate held at room temperature (microstructure just behind the surface)

For comparison, extrapolation of $N_o = 9 \times 10^{41} \exp(-0.153T)$ predicted a radius of 5.4 μm at 130 °C and 3.3 μm at 120 °C. Estimates of the lamellar thicknesses from the samples shown in Fig. 16 gave values of 7.2, 6.7 and 6.3 nm for crystallization temperatures of 172, 166 and 158 °C, respectively. If the lamellar thickness is assumed to scale as $1/\Delta T$, the thicknesses expected at 130 and 120 °C would be 5.7 and 5.65 nm, which is consistent with Fig. 17. Faster cooling by quenching a thin film in ice–water from the melt, on the other hand, led to no discernible features in the TEM or in the optical microscope.

There remains the question of the assumption of an induction time given by Eq. (11), which was necessary to account for both the isothermal and the nonisothermal data. However, if the dependence of N_o on T is assumed to be a consequence of athermal nucleation, as suggested elsewhere, it is difficult to account for the existence of an induction time at high undercooling [10, 11] and it is at present not possible to justify the form of Eq. (11). It is therefore of interest to consider the consequences of zero induction time. The corresponding crystallization onset as defined by 1% conversion is given by the hatched line in Fig. 15a. In this case, the apparent cooling rate necessary for quenching to a predominantly amorphous state is shifted from about 800 $\mathrm{Kmin^{-1}}$ to about 1000 $\mathrm{Kmin^{-1}}$.

Conclusions

The crystallization kinetics of PA-12 has been successfully modelled using a simple two-parameter Avrami model for isothermal crystallization, which has also been shown to be consistent with optical measurements of the spherulite growth rates and nucleation density. With small adjustments, parameters inferred from the isothermal DSC data also accounted for DSC data for nonisothermal crystallization, when the dynamic heat balance between the sample and the oven was taken into account. Further work is envisaged with the aim of investigating the balance between heterogeneous and homogeneous nucleation and the significance of the observed incubation times, and the role of the prior thermomechanical history on N_o.

Acknowledgement The authors acknowledge the financial support of the Swiss Priority Program for Materials.

References

1. Avrami MJ (1941) J Chem Phys 9:177
2. Avrami MJ (1940) J Chem Phys 8:212
3. Avrami MJ (1939) J Chem Phys 7:1103
4. Kolmogoroff AN (1937) Izv Akad Nauk Ser Math 3:335

5. Evans UR (1945) Trans Faraday Soc 41:365
6. Hillier IH (1965) J Polym Sci A 3:3067
7. Wu CH, Eder G, Janeschitz-Kriegl H (1993) Colloid Polym Sci 271:1116
8. Janeschitz-Kriegl H, Wippel H, Paulik C, Eder G (1993) Colloid Polym Sci 271:1107
9. Plummer CJG, Kausch H-H (1995) Colloid Polym Sci 273:227
10. Eder G, Janeschitz-Kriegl H (1997) In: Meijer HEN (ed) Materials science and technology, vol 18. Wiley-VCH, Weinheim, pp 269–342
11. Ziabicki A, Alfonso GC (1994) Colloid Polym Sci 272:1027
12. Warfield RW, Kayser MG, Hartmann B (1983) Makromol Chem 184:1927
13. Hoffman JD, Miller RL (1997) Polymer 38:3151
14. Hoffman JD, Davis GT, Lauritzen JI (1975) In: Hannay NB (ed) Treatise on solid state chemistry, vol 3. Plenum, New York, chapter 7
15. Brandrup J, Immergut EH (1989) Polymer handbook. Wiley, New York
16. Mandelkern L, Jain NL, Kim H (1968) J Polym Sci A-2 6:165
17. Van Krevelen DW (1976) Properties of polymers. Elsevier, Amsterdam
18. Hoffman JD, Weeks JJ (1962) J Chem Phys 37:1723
19. Gogolewski S, Gzerminiawska K, Gasiorek M (1980) Colloid Polym Sci 258:1130
20. Turnbull D, Fisher JC (1949) J Chem Phys 17:71
21. Lauritzen JI, Hoffman JD (1960) J Res Natl Bur Stand Sect A 64:73